Title:

High Spatial Resolution Ambient Ionization Mass Spectrometry Imaging Using Microscopy Image Fusion

Chih-Lin Chen, Li-En Lin, Ying-Chen Huang, Hsin-Hsiang Chung, Chiao-Wei Lin, Ko-Chien Chen, Yu-Ju Peng, Shih-Torng Ding, Tang-Long Shen, Cheng-Chih Hsu*

Author information

Chih-Lin Chen, Li-En Lin

These authors contributed equally to this work.

Affiliations

Department of Chemistry, National Taiwan University, No. 1, Sec. 4, Roosevelt Rd., Taipei 10617, Taiwan (R.O.C.)

Chih-Lin Chen, Li-En Lin, Ying-Chen Huang, Hsin-Hsiang Chung

Department of Plant Pathology and Microbiology, National Taiwan University, No. 1, Sec. 4, Roosevelt Rd., Taipei 10617, Taiwan (R.O.C.)

Ko-Chien Chen, Tang-Long Shen

Department of Animal Science and Technology, National Taiwan University, No. 1, Sec. 4, Roosevelt Rd., Taipei 10617, Taiwan (R.O.C.)

Yu-Ju Peng, Chiao-Wei Lin, Shih-Torng Ding

Corresponding author

Correspondence to Cheng-Chih Hsu (email: ccrhsu@ntu.edu.tw)

Abstract

Mass spectrometry imaging (MSI) using ambient ionization technique enables a direct chemical investigation of biological samples with minimal sample pretreatment. However, detailed morphological information of the sample is often lost due to its limited spatial resolution. We demonstrated that the fusion of ambient ionization MSI with optical microscopy of routine hematoxylin and eosin (H&E) staining produced predictive high-resolution molecular imaging. In this study, desorption electrospray ionization (DESI) and nanospray desorption electrospray ionization (nanoDESI) mass spectrometry were employed to visualize lipid and protein species on mouse tissue sections. The resulting molecular distributions obtained by ambient ionization MSI-microscopy fusion were verified with matrix-assisted laser desorption ionization time-of-flight (MALDI-TOF) MSI and immunohistochemistry (IHC) staining. Label-free molecular imaging with 5-µm spatial resolution can be achieved using DESI and nanoDESI, whereas the typical spatial resolution of ambient ionization MSI is ~100 µm. In this regard, sharpened molecular histology of tissue sections was achieved, providing complementary references to the pathology. Such multi-modality integration enabled the discovery of potential tumor biomarkers. After image fusion, we identified about 70% more potential biomarkers that could be used to determine the tumor margins on a lung tissue section with metastatic tumors.

Introduction

Image fusion combining spatially-resolved data from multiple analytical tools has been utilized to generate high quality images for better human interpretation[1]. A variety of image fusion methods, based on wavelet transform, morphology knowledge, artificial neural network, multivariate regression, and Pan-Sharpening methods, has been developed and successfully applied in different scientific fields[1–4]. For instance, it has been largely used for remote sensing and object recognition by merging the satellite imaging with high resolution panchromatic image to harvest more information[1,5]. One of the other successful applications of imaging fusion is in merging complementary medical images obtained with multiple modalities into one highly defined image for clinical analysis[4,6].

Mass spectrometry imaging (MSI) provides spatially resolved chemical information of the surface of biological samples in a

label-free manner, and has been profoundly used in preclinical, pharmaceutical and biological studies[7–15]. Furthermore, ambient ionization mass spectrometry imaging methods are capable of providing spatially resolved chemical information of cells and tissues with minimal sample pretreatment under atmospheric condition. In specific, the biological tissue sections that used for conventional pathological and molecular staining can be directly implemented for ambient ionization MSI at their intact states. Desorption electrospray ionization (DESI) and nanospray-desorption electrospray ionization (nanoDESI), were two of the most commonly used ambient ionization methods for *in-situ* analysis for different classes of compounds [10,11,16–22]. MSI using DESI and nanoDESI is of great potential as a complementary tool for pathological examinations in cancer diagnosis and has been largely used in determining the tumor margins[23–27]. In previous reports, lipid species had been widely studied and were served as important biomarkers to identify the malignant and benign tumor tissue by DESI MSI[23,24]. On the other hand, proteins were also reported to discriminate between normal tissues and tumors using nanoDESI MSI[11]. However, one of the challenges for clinical study by DESI and nanoDESI MSI is its spatial resolving power [28–31].

To visualize fine chemical details of the sample surface in its intact state comparable with conventional optical microscopy-based methods, the spatial resolution of ambient ionization MSI requires to improve[32]. Several instrumental approaches to increase the spatial resolution of ambient ionization MSI have been reported. For example, a hybrid atomic force microscopy mass spectrometer was applied for mapping bacterial colonies at sub-micrometer level under atmospheric pressure[33]. On the other hand, laser desorption/ablation-based methods allow imaging at subcellular level[34,35]. DESI is currently the most widely recognized ambient ionization methods for MSI. Although its lateral resolution can reach to about 10 μm with optimal parameter settings[36], the typical resolution of DESI MSI is about 100 μm. NanoDESI is known for its ability of *in-situ* protein MSI [10,11], but its spatial resolution is restricted by the instrumental design and occasional carried-over among pixels.

In addition to the instrumental approaches, numerical approaches, image fusion in particular, is an alternative strategy to surpass the inherent limitation of each ionization methods. Such strategy allows us to achieve a higher spatial resolution without using custom instruments or specialized experimental setup. Recently, Multivariate regression image fusion of optical or electron microscopy data with ultrahigh vacuum-based MSI, including matrix-assisted laser desorption ionization (MALDI) and secondary ion mass spectrometry (SIMS) MSI, were reported to achieve sharpened molecular imaging with spatial resolution at cellular level

on tissue sections[37,38,39]. Meanwhile, these MSI have to be operated under high vacuum conditions and may limit their compatibility with conventional imaging methods for pathological examinations.

In this study, an optical microscope was used to obtain images containing meticulous details of H&E stained tissue sections. Using multivariate regression algorithm, we fused ambient ionization MSI with optical microscopy so as to generate predictive MSI in different tissue types, and further used the fine-grained molecular mappings for cancer diagnosis. The workflow of our study is shown in Fig. 1 (see Supplementary Figure 1 for experimental setups), details of our results (see Supplementary Figure 2 for representative DESI and nanoDESI mass spectra), as well as experimental and data processing procedures (see Supplementary Figure 3 for the protocol of image fusion) are elaborated in the following sections.

Results

Lipid Mapping by DESI MSI with Elevated Spatial Resolution. The results for fusion of DESI MSI for mice brain and cerebellum coronal sections are shown in Fig. 2, whereas the results for mouse kidney sections were shown in Fig. 3 (see Supplementary Figure 4 and Supplementary Table 1 for compound identification using tandem mass analysis). For the raw lipid mappings in mice brain and cerebellum, as shown in Fig. 2b and 2e, the distribution of two phospholipids species, phosphatidylethanolamine (PE P-18:0/20:5) and phosphatidylcholine (PC 18:0/20:1) at *m/z* 772.5 and 838.6, respectively, were revealed by our raw DESI MSI at 150-μm resolution. PE (P-18:0/20:5) were largely found in the grey matter, whereas PC (18:0/20:1) were measured in the white matter, and similar distributions of these two phospholipids species in mammalian brains have been reported using DESI MSI[40,41]. Furthermore, in Fig. 3b and 3f, PE (P-18:0/20:5) and PC (16:0/16:0) distributed in the cortex, while the PC (16:0/18:1) distributed in the medulla of the kidney, where these results were also similar to the previous studies[42,43]. Although the DESI MSI provided a molecular imaging at sub-tissue level, in which different lipid species showed a drastic difference in their distribution in the brain, morphological details were missing due to its limitation in spatial resolution. After the fusion of DESI MSI with the optical microscopic image of the H&E staining using the same tissue sections, predictive molecular imaging of the denoted phospholipids were generated, showing much improved morphological details compared with

the raw DESI MSI. For example, the distribution of PE (P-18:0/20:5) from the raw DESI MSI only roughly revealed the hippocampus (Fig. 2b), while the predictive image (Fig. 2c) shows that PE (P-18:0/20:5) has lower abundance in the dentate gyrus. In the case of cerebellum (Fig. 2e and 2f), the originally pixelated molecular imaging was remarkably sharpened by image fusion, distinguishing between the cerebellar cortex and medulla. For the kidney sections in Fig. 3c and 3g, clear boundaries between the outer stripe of the outer medulla (OSOM) and the inner stripe of the outer medulla (ISOM) were drastically revealed after the image fusion, and their distribution were in agreement with the result obtained by MALDI-MSI using adjacent sections (Fig. 3d and 3h).

High-quality Protein Imaging by nanoDESI MSI. Unlike DESI, nanoDESI utilizes a micro-liquid junction sustained between two fused silica capillaries to desorb analyte compounds from the sample surfaces. This allows nanoDESI MSI to detect large biomolecules, e.g. proteins, with molecular weight up to 15 kDa[11,17,44]. However, as the stability of the micro-junction is sensitive to the flatness of the tissue sections, the carry-over of the analyte compounds among neighboring pixels in nanoDESI MSI is thus more significant than in DESI MSI, causing artifacts to the images and making it challenging to interpret. To expand the utility of image fusion to protein imaging, we applied nanoDESI MSI to mice tissue sections. As shown in Fig. 4, the spatial distribution of peak *m/z* 785.55 (+18 charge), annotated as myelin basic protein (MBP) using top-down tandem mass analysis (Supplementary Figure 5), was largely found on mice brain and mapped by nanoDESI MSI. Similar to the previous report , as MBP is highly expressed in the myelinated axons, it was profoundly observed in the white matter of the brain (Fig. 4b)[11]. After image fusion with the H&E stained adjacent section, a high-resolution image of MBP was thus generated (Fig. 4c). Remarkably, the severe tailing and cross-contamination of ion signals in the raw nanoDESI MSI due to carry-over effect was significantly eliminated in the predictive image. The distribution of MBP is well sharpened and in agreement with the histological features of the mice brain section. In order to prove the genuineness of the prediction using image fusion, a high resolution MALDI-TOF MSI was also implemented to the second adjacent sections. The resulting MALDI-TOF MSI (Fig. 4d) shows a very high similarity with the predictive image and thus verified that the pixel-wised carry-over was efficiently removed after image fusion.

In addition, the spatial distribution of hemoglobin subunit alpha (*m/z* 751.40) was successfully mapped in sagittal and coronal kidney sections as shown in Fig. 4f (see Supplementary Figure 6 for protein identification). The predictive image after

fusion with H&E stained sections exhibit that a large amount of hemoglobin subunit alpha was still located in the blood vessels and not smeared during the cryo-sectioning (Fig. 4g). The high-resolution MALDI-TOF MSI of the adjacent sections also verified this observation (Fig. 4h). Notably, due to the fact that the histological features of kidney change after few sections, a slight difference of the protein distribution obtained by nanoDESI MSI-microscopy fusion and MALDI-TOF MSI are expected.

Validations of Predicted MSI. We have demonstrated that DESI/nanoDESI MSI-microscopy image fusion provides an ability to resolve the molecular distribution of biomolecules on tissue sections at cellular level (~5 μm), which is comparable with the traditional immunohistochemical approaches. However, immunohistochemistry (IHC) staining requires pre-requisite knowledge to the target compounds, proteins in specific, and do not allows label-free analysis. Thus, to further demonstrate the capability of DESI/nanoDESI MSI-microscopy image fusion in resolving the distribution of biomolecules in a label-free manner, a series of adjacent mouse brain sections were prepared and sequentially analyzed (1) DESI, (2) nanoDESI MSI-microscopy fusion, (3) MALDI-TOF MSI, and (4) IHC staining microcopy for lipid and protein imaging (Fig. 5).

For lipid mapping shown in Fig. 5a-c, the *m/z* 774.5 was observed in the region of the cerebral cortex by DESI imaging. However, the boundary was blurred and unclear by DESI MSI (Fig. 5a) compared to the MALDI-TOF MSI (Fig. 5c). Meanwhile, after image fusion was incorporated, the structure of the brain section was resolved in the predictive high spatial resolution molecular image (Fig. 5b). For example, the hippocampus was unambiguously sketched in the mapping of this ion, showing comparable results with the MALDI-TOF MSI.

For protein detection shown in Fig. 5e-i, MBP (*m/z* 744.21, +19 charge) was visualized by nanoDESI MSI. The nominal spatial resolution (determined by the speed of translational stage and rate of data collection) of raw nanoDESI MSI was 200 μm, and the tissue histological details was relatively difficult to recognize due to the limited spatial resolution as a result of the large micro-junction radius and carry-over. In the raw nanoDESI MSI (Fig. 5e), the histochemical relationship of MBP was ambiguous, especially at the brain stem area. In Fig. 5i, the images at the retrosplenial cortex (purple) and the midbrain (red) are enlarged. After image fusion, MBP was predicted to be localized at the fiber tracts and fasciculus retroflexus (fr). Remarkably, similar results were obtained with MALDI MSI (Supplementary Figure 7). MBP is one of a major component of the myelin sheath. As a result, MBP can be easily detected in the white matter of a brain. To verify the result obtained our nanoDESI MSI, high-resolution

microscopic image of MBP was obtained by IHC staining of the neighboring tissue[45]. Unambiguously, we were able to observe highly comparable distributions of MBP from the results of nanoDESI MSI-microscopy image fusion and the conventional IHC staining, while eliminating complex and time-consuming sample pretreatment and the need for specific antibodies.

Image Fusion of DESI MSI for Improved Cancer Diagnosis. DESI MSI had been widely applied to study various cancer models[22–25,27], allowing us to delineate the tumor margins on a heterogeneous section at chemical level. Although ambient ionization MSI provides simple and rapid molecular evaluation of clinical specimens[46], its limited spatial resolution makes it difficult to assess small-size tumors, especially at the early stage or metastatic cancer. Failure in distinguishing cancer cells from benign tissue increase the likelihood for a second operation[47]. Thus, we seek to implement DESI MSI-microscopy image fusion to obtain greater details of molecular distribution in the cancer section. To evaluate its capability of predicting precise cancerous margin, we applied image fusion to obtain fine spatial resolution molecular imaging in breast cancer metastatic lung tissue sections (Fig. 6). The raw and predicted distributions of several phospholipids, including phosphatidylethanolamine (PE) and phosphatidylinositol (PI) were compared with the pathological examination (see Supplementary Figure 8 and Supplementary Table 2 for compound annotations). As elaborated in Fig. 6d, many of the tiny tumors are about the similar sizes with imaging pixels in the raw data, and thus no enough statistical estimations could be made to judge whether the denoted lipid species were observed or not. Meanwhile, the marker lipid, e.g. PI (20:4/18:0), was predicted to appear in the selected tiny tumors, suggesting that imaging fusion could be utilized to improve the performance of the ambient ionization MSI-based cancer diagnosis.

In addition, in order to determine whether the molecular distributions correlate with the cancer region in the tissue section, and to further verify if the predicted DESI MSI has greater performance in the mining of biomarker compounds, the receiver operating characteristic (ROC) curves were plotted for each raw molecular image (Supplementary Figure 9). ROC curve is a binary classifier and have been profoundly used in evaluating test for detections of cancers over the past decades[48–51]. In our study, spatial-chemical results of the metastatic lung section obtained by DESI MSI were compared with the pathological evaluations. We would like to highlight here that since DESI MSI is tissue-friendly, the same section could be reused for H&E staining and sent out for the routine pathology assessment. Subsequently, the ROC curves for each predicted molecular image were calculated and plotted as in Supplementary Figure 9, in which the ion with larger area under curve (AUC) of the ROC curve indicates that

the ion has greater potential to serve as an effective biomarker. On the other hand, ions having AUC of the ROC curves around 0.5, such as *m/z* 749.4 in Fig. 7a, represent that the distributions of the ion species were irrelevant to the presence of the tumors. In this regard, we defined the ions with AUC values > 0.7 as the potential biomarkers that can represent cancerous region in the tissue section. Using this criterion, we could found 16 ions with AUC of the ROC curves > 0.7, and the *m/z* values of these potential biomarkers were listed in Supplementary Table 3. For instance, as shown in Fig. 7a, the raw DESI MSI of *m/z* 743.4 ion had an AUC value ~ 0.77, indicating a high spatial correlation between the ion signal and pathological interpretation.

However, in the raw DESI MSI, the distribution of the ions had obscure outlines and thus it is difficult to differentiate the malignant tissue from normal one. Therefore, some potential biomarkers were neglected. As have been demonstrated previously, the outline of the ions was sharpened after image fusion, making it easier to determine the tumor margins. In specific, as shown in Supplementary Figure 9, the ROC curves are bended more off-diagonally, meaning that the strengths of the classifiers are increased. More importantly, many of the ineffective markers (ions that have AUC values between 0.5 to 0.7) in raw MSI were then be able to be recognized as effective biomarkers (AUC values > 0.7) in the predictive MSI. For example, as shown in Fig. 7b, the AUC of *m/z* 724.6 ion increased from 0.65 to 0.79 after image fusion, making it a new potential biomarker of the tumor. This demonstrated the power of microscopy-DESI MSI in consolidating the effectiveness of molecular classifier to cancer assessment. In fact, by utilizing the greatly improved molecular mapping of high resolution microscopy-DESI MSI, 11 new ion species (equivalent to ~68% of the original number) were recognized as potential biomarkers, and the total number of biomarkers increased from 16 in raw MSI to 27 in the predicted MSI. The list of these biomarkers was elaborated in the supporting information Supplementary Table 3.

Discussion

The development of ambient ionization MSI in the past decade has pushed the boundary of cancer diagnosis to the chemical level[10,15,22–25,27,52]. As the tissue samples can be investigated directly under atmospheric pressure with only minimal sample preparation, it allows the integration of pathological examination and biomolecular mapping in a single section. However, due to its instrument limitation in spatial resolving power, a lot of biological information is missing in ambient ionization MSI. Although

the near-cellular resolution could be achieved with optimal instrument settings, to obtained the similar ion intensity and signal-to-noise ratio as in low resolution MSI, the acquisition time required for MSI becomes enormous because fewer target compounds are left in smaller pixels. In addition, when the spatial resolution of an MSI is doubled, the overall scanning time is consequently quadrupled. Longer scanning time also represents more serious compound degradation during imaging. Since the chemical compositions of the sample are altered as the it is exposed to the ambient environment, minimizing the acquisition time of MSI is thus crucial[53]. Utilizing numerical image fusion allows not only an improved MSI quality but also a higher data throughput, since intensive scanning is no longer required. As such, an optical microscopy-ambient ionization MSI was proposed and implemented to generate predictive MSI with a lateral resolution of the conventional optical microscopic data. We were able to extract the biological details to make a chemically-rich, high spatially-resolved image from a single tissue section, that is compatible with both the routine histological protocol and MSI.

In conclusion, we showed that the image fusion of DESI and nanoDESI MSI with H&E staining microscopy image was able to generate predictive imaging of biomolecules in various tissue sections. The morphological details were revealed in the high resolution MSI on mice brain, cerebellum, and kidney sections. More importantly, the predictive lipid and protein images were further validated by the comparison with MALDI MSI and conventional IHC staining microscopy. The unambiguous prediction by microscopy-ambient ionization MSI allowed a more precise determination of tumor margins and deeper mining of cancer biomarkers. Using a metastatic lung tissue section as a proof-of-concept, we disclosed more than 10 new ion species that could serve as potential tumor biomarkers. As it is nicely compatible with the routine histological protocols and pathological evaluations, image fusion of ambient ionization MSI with H&E staining microscopy images showed a great possibility for future applications in clinical diagnosis. We believe that our results have contributed towards this end.

Methods

Tissue sample preparation. Mice brain and kidney tissues were purchased from BioLASCO Taiwan Co., Ltd. Gender and age of the ICR mice were not specified. Metastatic lung tissues derived from MMTV-PyMT breast cancer mice model were collected from the laboratory of Dr.

Tang-Long Shen (National Taiwan University) and the experimental details were described elsewhere[54,55]. All experimental procedures were handled in accordance with the protocols and the ethical regulations approved by the Institutional Animal Care and Use Committee of National Taiwan University (IACUC approval NO. NTU104-EL-00003). The intact organs were harvested as soon as euthanasia and then stored under -80˚C prior cryo-sectioning. For tissue cryo-sectioning, organs were flash-frozen using liquid nitrogen and kept under -20˚C in the cold tome (LEICA, CM1900) in order to reach the optimal temperature before sectioning. Tissue samples were sectioned to 14-µm thick sections and thaw-mounted onto the slides and stored at -80˚C prior to analysis without fixation. Slides used for nanoDESI MSI analysis were regular plain glass without any coating. For DESI, H&E staining and immunostaining, tissues were thaw-mounted onto silane coated slides; while the slides for MALDI analysis were coated with indium tin oxide. Before nanoDESI MS interrogation, tissue sections were dried in a dissector for ~1 hour and then rinsed with 50 ml of chloroform for 1 min. Adjoining tissue section pretreatment for MALDI validation is as described in the following. The matrix application was achieved by sublimation method, which has been described elsewhere[56], followed by a recrystallization step[57]. The sublimation apparatus was purchased from Singlong (Taichung, Taiwan) and placed in a sand bath on a hot plate while applying matrix. The brain sections were adhered to ITO-coated glass slides by a conductive tape and stored under -80°C before applying matrix. Sublimation was performed using 2,5-dihydroxyacetophenone (2,5-DHA). The matrix sublimation and application were performed at 110 °C with a 0.7 Torr vacuum for 10 minutes. Amount of the applied matrices were determined by the exposure time. The matrix-coated samples were rehydrated with 50% TFA solution in an incubator at 37 °C for 4 minutes. A sonication step was added to increase the signal for protein analysis[58]. The sonication was operated by Elmasonic S 30 H ultrasonicator under continuous mode with frequency of 37 KHz. As for DESI MS interrogation, tissue sections were dried in a dissector for ~1 hour, no further sample pretreatment was conducted before analysis.

Ambient ionization mass spectrometry imaging. For DESI MSI, commercial DESI source (Prosolia Inc., IN, USA) was mounted to Orbitrap

Elite to conduct the MSI measurements. The gas pressure of nitrogen was set at 150 psi, the angle of the spray head was set to 55˚, the flow rate of the solvent (DMF:ACN = 1:1) was 2 µl/min and the voltage was 3.5 kV. The nanoDESI system was modified from the commercial DESI platform, in which two flame-pulled fused capillaries (O.D: 360µm, I.D: 250 µm) were implanted and used to substitute the original DESI emitter. The solvent delivery (primary) capillary (65% ACN with 1% formic acid), was applied with a high voltage (2.5kV) to extract and ionize the compound on the surface of the sample. The secondary capillary was used to deliver the extracts from the sample to the mass spectrometer. The MSI experiments were conducted using Prosolia's DESI 2D system. The scanning rates of the motor stage for DESI and nanoDESI MSI were set approximate 150 µm s^{-1} and 30 µm s^{-1}, respectively. The acquired raw data were then imported into Firefly™ 2.2 for data conversion, then we imported the converted data into BioMAP to obtain the final DESI and nanoDESI MSI. For H&E staining, the tissue slides were rinsed with 70% EtOH and then 100% EtOH for 30 sec each and allow dry under vacuum. The hematoxylin staining was applied under 60˚C for 40 sec. After hematoxylin staining, the slides were rinsed with H_2O, then rinsed with acidified EtOH 0.3% for 3 sec, then rinsed with H_2O. The bluing up was achieved by 1% NH_4OH and finally H_2O under room temperature. Then the slides were dipped into the eosin stain for 20 sec, then the slides were rinsed with H_2O, then 80% EtOH, then 90% EtOH, and finally 99% EtOH at room temperature.

Image fusion data pretreatment. The MSI data was converted into .img file by Firefly™ 2.2 and exported into a built-in matlab package MSiReader. The region of interest for each datasets was determined empirically by overlapping the H&E image and the MSI data in MSiReader[59]. The signals were binned into 2,000 bins and summed before exported as uniformly spaced text file. The microscope images were collected by an optical microscope (WHITED INC., Taipei, Taiwan) with a PSC600-05C digital camera (OPLENIC CORP., USA) and data processed by AOR AJ-VERT. The microscopy images were then exported as a uniform data array by in-house generated Matlab script. An affine transform matrix that can describe the spatial relationship between MSI data and microscopy data was calculated using an in-house generated

script. The alignment of the data sets was done by aligning upsampled MSI data and the microscopic data to ensure the best fitting. In detail, three pixels in the MSI were selected for the teaching point setting. The image of the MSI was interpolated by dividing each pixel into 36 smaller sub-pixels (6*6 sub-pixels per original pixel) and the four sub-pixels at the center were colored. The upsampled MSI data was aligned with the microscopic image manually by adjusting the transparency of both images. The teaching points on the microscopy image were determined by the center of the colored sub-pixels on the upsampled MSI image.

The processed data was exported by in-house generated Matlab script and imported into "Molecular image fusion system" under command-line interface.

Receiver operating characteristic curve. The ROC curve and AUC was constructed by in-house generated MATLAB code. It is composed of the sensitivity and (1-specificity) when using different intensity thresholds to determine the classification of tissue. If the intensity of a specific *m/z* peak in a particular pixel was higher than the intensity threshold, the pixel was then considered as cancer. Otherwise, the pixel was assigned as normal. After that, the results were compared with H&E stained metastatic lung tissue image labelled by the pathologist to calculate the sensitivity and specificity of this ion. The sensitivity was the percentage that the "cancer" pixels label by the pathologist was agreed by the molecular imaging; The (1-specificity) was the percentage that the normal tissue was marked as "cancer" in the molecular imaging. The curves were sketched by setting the intensity threshold from 0% to 100% of the highest intensity. Images with reconstruction score > 78% were evaluated.

Conventional high resolution molecular imaging. All the procedures for immunostaining are based on the description of the commercial kit (TAHC03, BioTnA, Kaohsiung, Taiwan). After immunostaining, the slides were mounted and digitized with an Motic Easyscan Digital Slide Scanner (Motic Hong Kong Limited, Hong Kong, China) at ×40 (0.26 μm/pixel) with high precision (High precision autofocus). Motic Easyscan

whole-slide images were viewed with DSAssistant and EasyScanner software at Litzung Biotechnology INC (Kaohsiung, Taiwan). Matrix-assisted laser desorption/ionization mass spectrometry images were acquired using MALDI-TOF/TOF mass spectrometry (Autoflex Speed MALDI TOF/TOF system, Bruker Daltonics). The instrument was equipped with the third harmonic of Nd:YAG SmartBeamTM-II laser (355nm). Imaging spectra were recorded and processed by flexControl 3.4 and flexImaging 3.0 (Bruker Daltonics). The spectra were acquired in positive polarity with pixel-to-pixel resolution of 60µm using the following parameters: laser attenuator offset at 80% of the maximum power; laser operating power at 90% under linear mode for protein analysis and 80% under reflectron mode for lipid analysis with smartbeam parameter at 2_small; laser repetition rate at 1 kHz; acquisition shots accumulated to 1,000 shots per pixel for imaging analysis. The resulting imaging spectra were processed using TopHat baseline subtraction and normalized to the total ion counts per pixel.

Mass spectrometry-based molecular identifications. Protein identifications was done by top-down protein analysis. Protein ions were directly introduced to the LTQ Orbitrap Elite using the same platform for tandem mass analysis, protein of interest was chosen as the mass center of 5 *m/z* isolation window with an activation energy Q of 0.25 and utilize collision energy of 30%. The data was imported into Prosight PTM for identification[60,61]. Lipid identifications were done by high performance liquid chromatography–tandem mass spectrometry analysis. Brain tissue was extracted with MTBE methods[62]. The HPLC-MS/MS analysis was performed using HPLC (LC-20AD, Shimadzu, Tokyo, Japan), coupled with Orbitrap Elite (Thermo Scientific). HPLC experiments were performed using C18 column (100*2.1mm, 3.5µm, Agilent) and following the gradient elution: mobile phase A= water with 0.1% formic acid (v/v); mobile phase B= acetonitrile and isopropanol (10:90, v/v) with 0.1 % formic acid (v/v); elution profile= 0.0-5.0 min (40% mobile phase B); 5.0-35.0 min (40-90% mobile phase B); 35.0-50.0 min (90% mobile phase B), column oven at 25°C, volume injection 10 µL and flow rate of 0.15 mL/min. Mass spectrometry acquisition parameters were as followed: positive ions mode, heater temperature 180°C, sheath gas flow rate 35 arb, auxiliary gas flow rate 10 arb, sweep gas flow rate 10 arb, spray

voltage 3.5 kV and capillary temperature 350°C. CID fragmentation was performed for targeting ion peaks observed in DESI analysis with collision energy of 30% and an activation Q of 0.25. The MS spectra were collected in FT mode with 30,000 resolving power. The mass spectral analysis was processed by Xcalibur QualBrowser.

Data and code availability. The mass spectrum for MS/MS annotations are included in the Supplementary information. Other materials and MATLAB code are available from the corresponding author upon reasonable request.

References

1. Pohl, C. & Genderen, J. L. V. Review article Multisensor image fusion in remote sensing: Concepts, methods and applications. *Int. J. Remote Sens.* **19**, 823–854 (1998).
2. Xydeas, C. S. & Petrovic, V. Objective image fusion performance measure. *Electron. Lett.* **36**, 308–309 (2000).
3. Li, H., Manjunath, B. S. & Mitra, S. K. Multisensor Image Fusion Using the Wavelet Transform. *Graph. Models Image Process.* **57**, 235–245 (1995).
4. James, A. P. & Dasarathy, B. V. Medical image fusion: A survey of the state of the art. *Inf. Fusion* **19**, 4–19 (2014).
5. Ma, J., Ma, Y. & Li, C. Infrared and visible image fusion methods and applications: A survey. *Inf. Fusion* **45**, 153–178 (2019).
6. Ghassemian, H. A review of remote sensing image fusion methods. *Inf. Fusion* **32**, 75–89 (2016).
7. Khatib-Shahidi, S., Andersson, M., Herman, J. L., Gillespie, T. A. & Caprioli, R. M. Direct Molecular Analysis of Whole-Body Animal Tissue Sections by Imaging MALDI Mass Spectrometry. *Anal. Chem.* **78**, 6448–6456 (2006).
8. Wiseman, J. M. *et al.* Desorption electrospray ionization mass spectrometry: Imaging drugs and metabolites in tissues. *Proc.*

Natl. Acad. Sci. U. S. A. **105**, 18120–18125 (2008).

9. Trim, P. J. *et al.* Matrix-Assisted Laser Desorption/Ionization-Ion Mobility Separation-Mass Spectrometry Imaging of Vinblastine in Whole Body Tissue Sections. *Anal. Chem.* **80**, 8628–8634 (2008).

10. Hsu, C.-C. & Dorrestein, P. C. Visualizing life with ambient mass spectrometry. *Curr. Opin. Biotechnol.* **31**, 24–34 (2015).

11. Hsu, C.-C., Chou, P.-T. & Zare, R. N. Imaging of Proteins in Tissue Samples Using Nanospray Desorption Electrospray Ionization Mass Spectrometry. *Anal. Chem.* **87**, 11171–11175 (2015).

12. Gouw, A. M. *et al.* Oncogene KRAS activates fatty acid synthase, resulting in specific ERK and lipid signatures associated with lung adenocarcinoma. *Proc. Natl. Acad. Sci.* **114**, 4300–4305 (2017).

13. Ifa, D. R. & Eberlin, L. S. Ambient Ionization Mass Spectrometry for Cancer Diagnosis and Surgical Margin Evaluation. *Clin. Chem.* **62**, 111–123 (2016).

14. Sans, M., Feider, C. L. & Eberlin, L. S. Advances in mass spectrometry imaging coupled to ion mobility spectrometry for enhanced imaging of biological tissues. *Curr. Opin. Chem. Biol.* **42**, 138–146 (2018).

15. Zhang, J. *et al.* Cardiolipins Are Biomarkers of Mitochondria-Rich Thyroid Oncocytic Tumors. *Cancer Res.* **76**, 6588–6597 (2016).

16. Takáts, Z., Wiseman, J. M., Gologan, B. & Cooks, R. G. Mass Spectrometry Sampling Under Ambient Conditions with Desorption Electrospray Ionization. *Science* **306**, 471–473 (2004).

17. Hsu, C.-C. *et al.* Real-time metabolomics on living microorganisms using ambient electrospray ionization flow-probe. *Anal. Chem.* **85**, 7014–7018 (2013).

18. Roach, P. J., Laskin, J. & Laskin, A. Nanospray desorption electrospray ionization: an ambient method for liquid-extraction surface sampling in mass spectrometry. *Analyst* **135**, 2233–2236 (2010).

19. Lane, A. *et al.* Desorption electrospray ionization mass spectrometry reveals surface-mediated antifungal chemical defense of a tropical seaweed. *Proc. Natl. Acad. Sci. U. S. A.* **106**, 7314–9 (2009).

20. Laskin, J., Heath, B. S., Roach, P. J., Cazares, L. & Semmes, O. J. Tissue Imaging Using Nanospray Desorption Electrospray Ionization Mass Spectrometry. *Anal. Chem.* **84**, 141–148 (2012).

21. Kauppila, T. J. *et al.* Desorption electrospray ionization mass spectrometry for the analysis of pharmaceuticals and metabolites. *Rapid Commun. Mass Spectrom. RCM* **20**, 387–392 (2006).

22. Takáts, Z., Wiseman, J. M. & Cooks, R. G. Ambient mass spectrometry using desorption electrospray ionization (DESI): instrumentation, mechanisms and applications in forensics, chemistry, and biology. *J. Mass Spectrom.* **40**, 1261–1275 (2005).

23. Banerjee, S. *et al.* Diagnosis of prostate cancer by desorption electrospray ionization mass spectrometric imaging of small metabolites and lipids. *Proc. Natl. Acad. Sci. U. S. A.* **114**, 3334–3339 (2017).

24. Eberlin, L. S. *et al.* Classifying Human Brain Tumors by Lipid Imaging with Mass Spectrometry. *Cancer Res.* **72**, 645–654 (2012).

25. Zhang, J. *et al.* Nondestructive tissue analysis for ex vivo and in vivo cancer diagnosis using a handheld mass spectrometry system. *Sci. Transl. Med.* **9**, eaan3968 (2017).

26. McDonnell, L. A. *et al.* Peptide and protein imaging mass spectrometry in cancer research. *J. Proteomics* **73**, 1921–1944 (2010).

27. Eberlin, L. S. *et al.* Molecular assessment of surgical-resection margins of gastric cancer by mass-spectrometric imaging. *Proc. Natl. Acad. Sci. U. S. A.* **111**, 2436–2441 (2014).

28. Schwamborn, K. & Caprioli, R. M. Molecular imaging by mass spectrometry — looking beyond classical histology. *Nat. Rev. Cancer* **10**, 639–646 (2010).

29. Rao, W., Pan, N., Tian, X. & Yang, Z. High-Resolution Ambient MS Imaging of Negative Ions in Positive Ion Mode: Using Dicationic Reagents with the Single-Probe. *J. Am. Soc. Mass Spectrom.* **27**, 124–134 (2016).

30. Rae Buchberger, A., DeLaney, K., Johnson, J. & Li, L. Mass Spectrometry Imaging: A Review of Emerging Advancements and Future Insights. *Anal. Chem.* **90**, 240–265 (2018).

31. Cooks, R. G., Ouyang, Z., Takats, Z. & Wiseman, J. M. Ambient Mass Spectrometry. *Science* **311**, 1566–1570 (2006).

32. McDonnell, L. A. & Heeren, R. M. A. Imaging mass spectrometry. *Mass Spectrom. Rev.* **26**, 606–643 (2007).

33. Ovchinnikova, O. S., Kjoller, K., Hurst, G. B., Pelletier, D. A. & Van Berkel, G. J. Atomic Force Microscope Controlled Topographical Imaging and Proximal Probe Thermal Desorption/Ionization Mass Spectrometry Imaging. *Anal. Chem.* **86**, 1083–1090 (2014).

34. Kim, J. Y. *et al.* Atmospheric pressure mass spectrometric imaging of live hippocampal tissue slices with subcellular spatial resolution. *Nat. Commun.* **8**, 2113 (2017).

35. Lee, J. K., Jansson, E. T., Nam, H. G. & Zare, R. N. High-Resolution Live-Cell Imaging and Analysis by Laser Desorption/Ionization Droplet Delivery Mass Spectrometry. *Anal. Chem.* **88**, 5453–5461 (2016).

36. Kertesz, V. & Van Berkel, G. J. Improved imaging resolution in desorption electrospray ionization mass spectrometry. *Rapid*

Commun. Mass Spectrom. RCM **22**, 2639–2644 (2008).

37. Van de Plas, R., Yang, J., Spraggins, J. & Caprioli, R. M. Image fusion of mass spectrometry and microscopy: a multimodality paradigm for molecular tissue mapping. *Nat. Methods* **12**, 366–372 (2015).

38. Neumann, E. K. *et al.* Multimodal Chemical Analysis of the Brain by High Mass Resolution Mass Spectrometry and Infrared Spectroscopic Imaging. *Anal. Chem.* **90**, 11572–11580 (2018).

39. Vollnhals, F. *et al.* Correlative Microscopy Combining Secondary Ion Mass Spectrometry and Electron Microscopy: Comparison of Intensity–Hue–Saturation and Laplacian Pyramid Methods for Image Fusion. *Anal. Chem.* **89**, 10702–10710 (2017).

40. Jarmusch, A. K. *et al.* Differential Lipid Profiles of Normal Human Brain Matter and Gliomas by Positive and Negative Mode Desorption Electrospray Ionization – Mass Spectrometry Imaging. *PLOS ONE* **11**, e0163180 (2016).

41. Martínez-Gardeazabal, J. *et al.* Lipid mapping of the rat brain for models of disease. *Biochim. Biophys. Acta BBA - Biomembr.* **1859**, 1548–1557 (2017).

42. Vidová, V. *et al.* Laser Desorption-Ionization of Lipid Transfers: Tissue Mass Spectrometry Imaging without MALDI Matrix. *Anal. Chem.* **82**, 4994–4997 (2010).

43. Römpp, A., Guenther, S., Takats, Z. & Spengler, B. Mass spectrometry imaging with high resolution in mass and space (HR2 MSI) for reliable investigation of drug compound distributions on the cellular level. *Anal. Bioanal. Chem.* **401**, 65–73 (2011).

44. Hsu, C.-C. *et al.* Top-Down Atmospheric Ionization Mass Spectrometry Microscopy Combined With Proteogenomics. *Anal. Chem.* **89**, 8251–8258 (2017).

45. Ramos-Vara, J. A. & Miller, M. A. When Tissue Antigens and Antibodies Get Along: Revisiting the Technical Aspects of Immunohistochemistry—The Red, Brown, and Blue Technique. *Vet. Pathol.* **51**, 42–87 (2014).

46. Zhang, J. *et al.* Detection of Metastatic Breast and Thyroid Cancer in Lymph Nodes by Desorption Electrospray Ionization Mass Spectrometry Imaging. *J. Am. Soc. Mass Spectrom.* **28**, (2017).

47. Lopez-Garcia, M. A., Geyer, F. C., Lacroix-Triki, M., Marchió, C. & Reis-Filho, J. S. Breast cancer precursors revisited: molecular features and progression pathways. *Histopathology* **57**, 171–192 (2010).

48. Hajian-Tilaki, K. Receiver Operating Characteristic (ROC) Curve Analysis for Medical Diagnostic Test Evaluation. *Casp. J. Intern. Med.* **4**, 627–635 (2013).

49. Klein, O. *et al.* MALDI imaging mass spectrometry: Discrimination of pathophysiological regions in traumatized skeletal muscle by characteristic peptide signatures. *PROTEOMICS* **14**, 2249–2260 (2014).

50. Hulme, H. E. *et al.* Mass spectrometry imaging identifies palmitoylcarnitine as an immunological mediator during Salmonella Typhimurium infection. *Sci. Rep.* **7**, 2786 (2017).

51. Patterson, N. H. *et al.* Assessment of pathological response to therapy using lipid mass spectrometry imaging. *Sci. Rep.* **6**, 36814 (2016).

52. Laskin, J. & Lanekoff, I. Ambient Mass Spectrometry Imaging Using Direct Liquid Extraction Techniques. *Anal. Chem.* **88**, 52–73 (2016).

53. Prentice, B. M. & Caprioli, R. M. The Need for Speed in Matrix-Assisted Laser Desorption/Ionization Imaging Mass Spectrometry. *Postdoc J. J. Postdr. Res. Postdr. Aff.* **4**, 3–13 (2016).

54. Guy, C. T., Cardiff, R. D. & Muller, W. J. Induction of mammary tumors by expression of polyomavirus middle T oncogene: a transgenic mouse model for metastatic disease. *Mol. Cell. Biol.* **12**, 954–961 (1992).

55. Luo, M. *et al.* Mammary Epithelial-Specific Ablation of the Focal Adhesion Kinase Suppresses Mammary Tumorigenesis by Affecting Mammary Cancer Stem/Progenitor Cells. *Cancer Res.* **69**, 466–474 (2009).

56. Hankin, J. A., Barkley, R. M. & Murphy, R. C. Sublimation as a Method of Matrix Application for Mass Spectrometric Imaging. *J. Am. Soc. Mass Spectrom.* **18**, 1646–1652 (2007).

57. Yang, J. & Caprioli, R. M. Matrix Sublimation/Recrystallization for Imaging Proteins by Mass Spectrometry at High Spatial Resolution. *Anal. Chem.* **83**, 5728–5734 (2011).

58. Lin, L.-E., Su, P.-R., Wu, H.-Y. & Hsu, C.-C. A Simple Sonication Improves Protein Signal in Matrix-Assisted Laser Desorption Ionization Imaging. *J. Am. Soc. Mass Spectrom.* **29**, 796–799 (2018).

59. Robichaud, G., Garrard, K. P., Barry, J. A. & Muddiman, D. C. MSiReader: an open-source interface to view and analyze high resolving power MS imaging files on Matlab platform. *J. Am. Soc. Mass Spectrom.* **24**, 718–721 (2013).

60. LeDuc, R. D. & Kelleher, N. L. Using ProSight PTM and Related Tools for Targeted Protein Identification and Characterization with High Mass Accuracy Tandem MS Data. *Curr. Protoc. Bioinforma.* **19**, 13.6.1-13.6.28 (2007).

61. Zamdborg, L. *et al.* ProSight PTM 2.0: improved protein identification and characterization for top down mass spectrometry. *Nucleic Acids Res.* **35**, W701-706 (2007).

62. Matyash, V., Liebisch, G., Kurzchalia, T. V., Shevchenko, A. & Schwudke, D. Lipid extraction by methyl-tert-butyl ether for high-throughput lipidomics. *J. Lipid Res.* **49**, 1137–1146 (2008).

Additional information

Acknowledgments

This research was supported by Ministry of Science and Technology (MOST), R.O.C. (Grant nos.: MOST 106-2113-M-002-013-MY2, 107-2321-B-001-038-, and 108-2636-M-002-008-), and Center for Emerging Materials and Advanced Devices, National Taiwan University (NTU) (Grant nos.: NTU-ERP-108L880116). Li-En Lin was supported by MOST grant 106-2813-C-002-136-M. The instrument support from NTU Mass Spectrometry Platform was acknowledged. The laboratory services of histology and pathology by the experienced veterinary pathologist, Hao-Kai Chang, at Litzung Biotechnology Inc., Taiwan, was acknowledged.

Author Contributions

C.L.C., L.E.L., Y.C.H. and H.H.C. conducted experiments; C.L.C., L.E.L. and H.H.C. performed data processing; C.L.C., L.E.L. and C.C.H. conceived and designed the research; C.L.C., L.E.L. and C.C.H. wrote the article. All authors have read and approved the final manuscript.

Competing interests

The authors declare no competing financial interests.

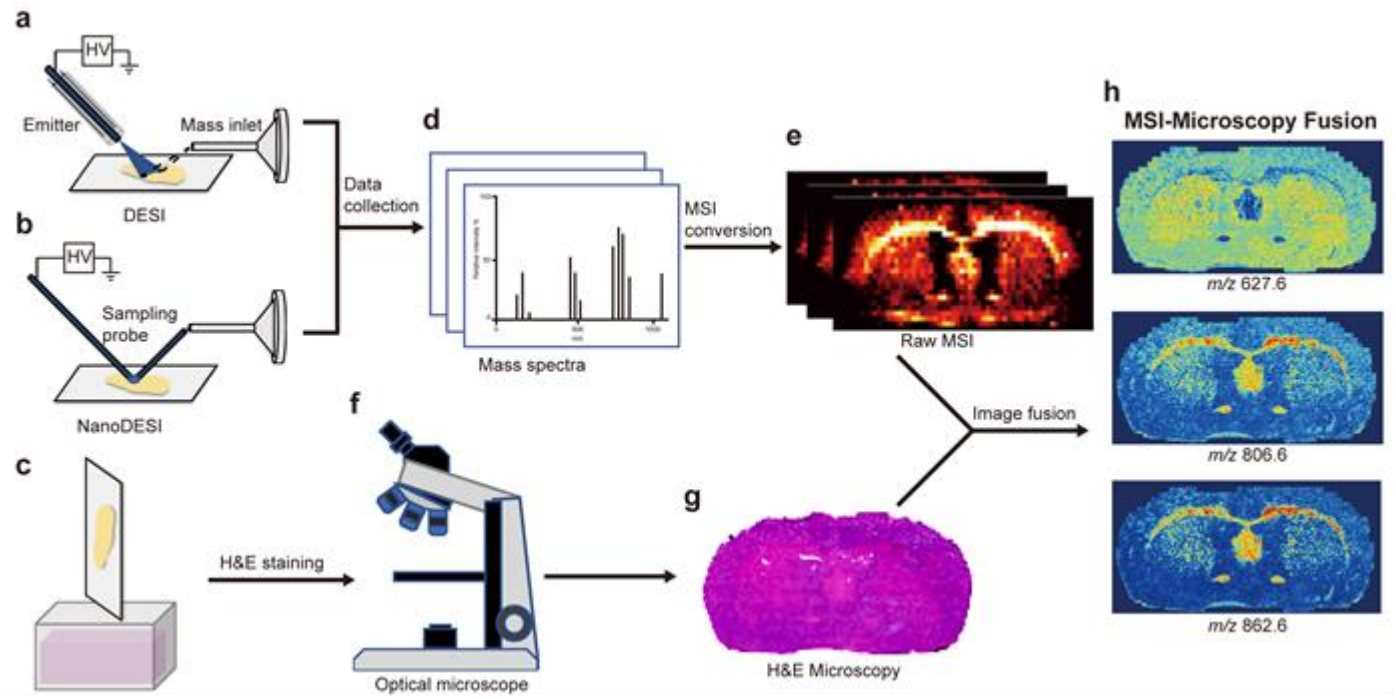

Fig. 1 Illustration of the ambient ionization data acquisition and mass spectra image fusion process. (a) Scheme of desorption electrospray ionization setup. (b) Homemade nanospray desorption electrospray ionization source. (c), (f), (g) H&E stained serial sections microscopy image acquisition procedure. (d) MS data collection from ambient ionization sources. (e) Peak based serial MS images. After MSI data collection from the ambient ionization sources, optical microscopies of H&E stained residue (for DESI) or adjacent (for nanoDESI) sections were employed for chemical spatial distribution prediction based on statistic measurement to profile higher spatial resolution molecular distributions.

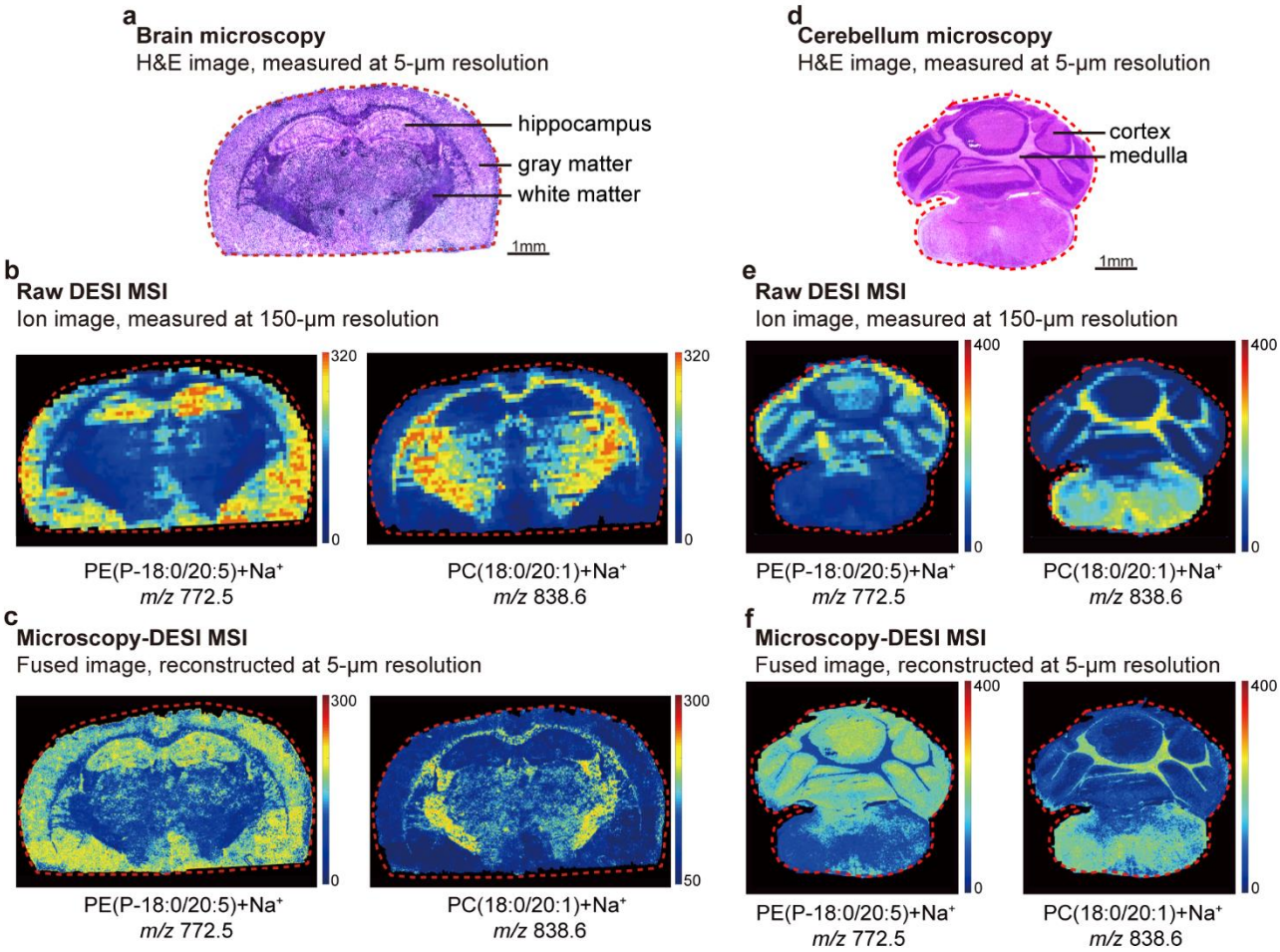

Fig. 2 Lipid distribution of brain and cerebellum mapped by DESI MSI. (a) H&E stained brain section. (b) Raw DESI-MSI of lipid species. (c) Predicted high spatial resolution MSI after applying mage fusion. (d) H&E stained cerebellum section. (e) Raw DESI-MSI of lipid species. (f) Predicted high spatial resolution MSI after applying image fusion. Small molecules such as lipid were ionized using DESI and carried to the mass spectrometry by secondary droplets.

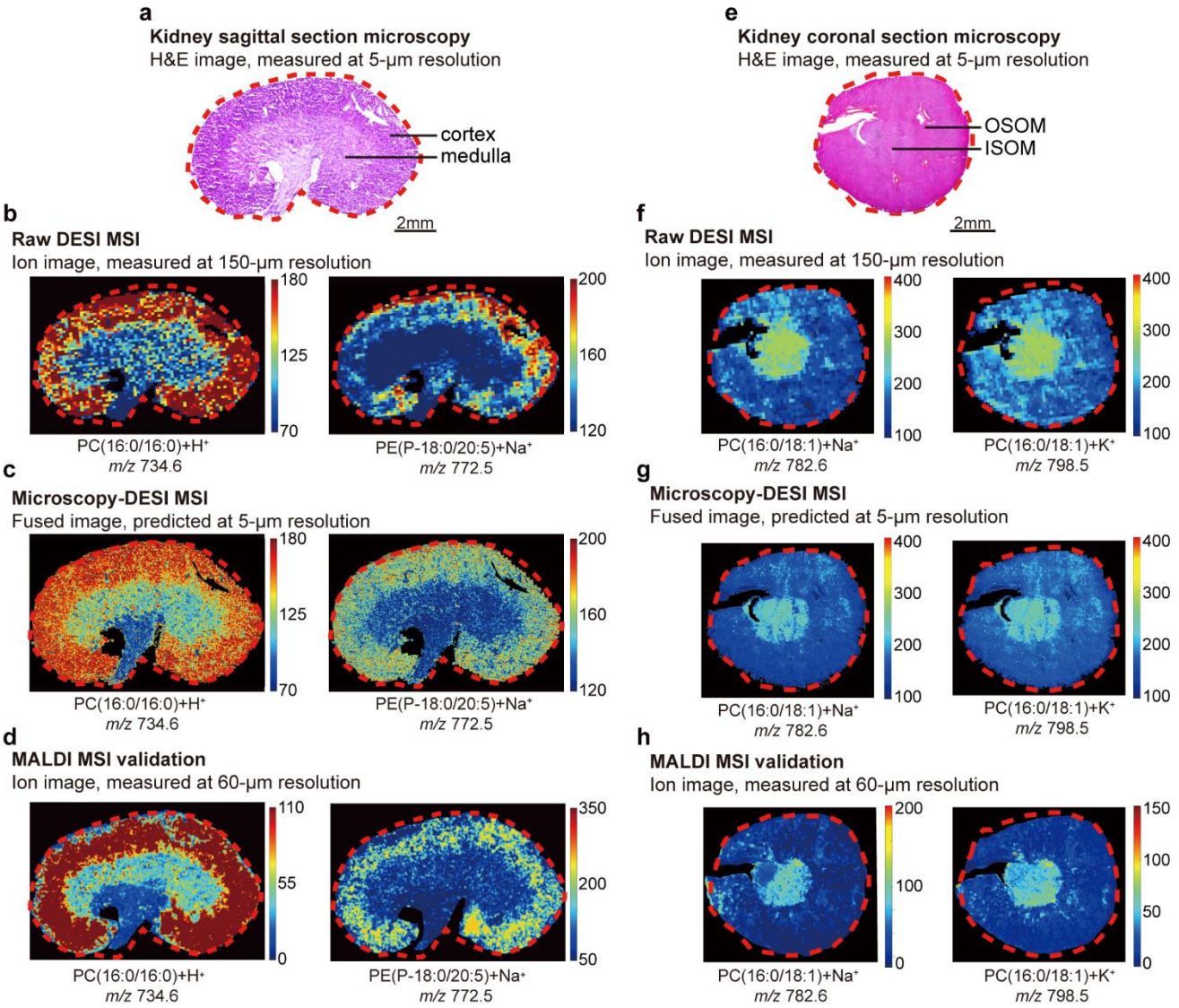

Fig. 3 Lipid distribution of kidney sagittal and coronal sections by DESI and MALDI analysis. (a) Sagittal section of mouse kidney. (b) Raw DESI MSI visualized lipid protonated and sodium adducts of PC (16:0/16:0) and PE(P-18:0/20:5), respectively. (c) Predicted high spatial resolution MSI after applying image fusion. (d) Adjoining sections of kidney sagittal sections mapped by MALDI MSI for distribution of lipid species. (e) Coronal section of mouse kidney. (f) Raw DESI MSI visualized same lipid PC (16:0/18:1) sodium and potassium adducts local distribution, respectively. (g) Predicted high spatial resolution MSI after applying image fusion. (h) Adjoining sections of kidney coronal sections mapped by MALDI MSI for distribution of lipid species.

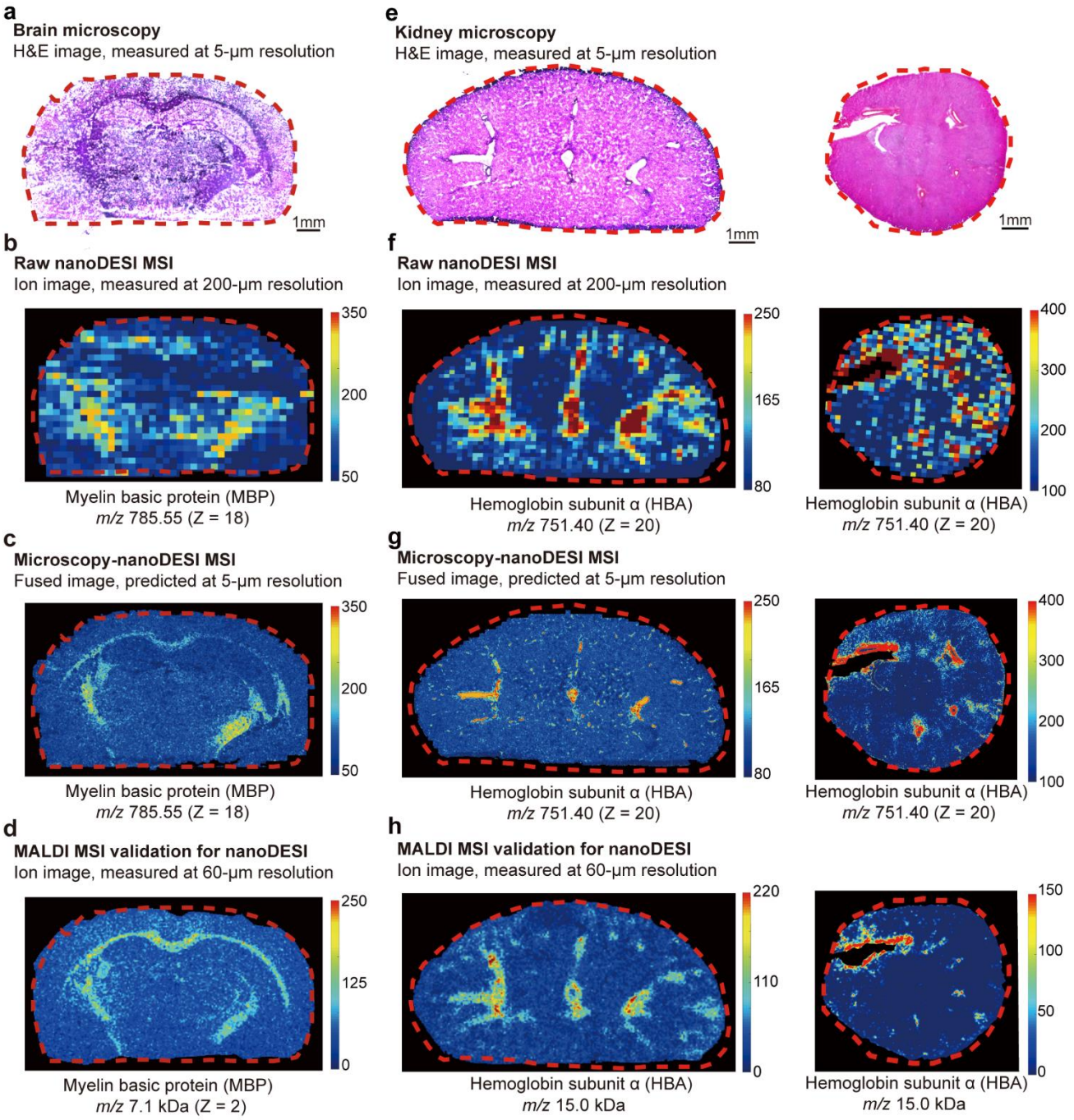

Fig. 4 Protein distribution of brain and kidney sections by nanoDESI and MALDI analysis. (a) H&E stained adjacent brain tissue of nanoDESI analysis. (b) Raw DESI MSI visualized MBP at 200 μm spatial resolution. (c) Predicted high spatial resolution molecular distribution of MBP after applying image fusion. (d) Adjoining sections of brain sections mapped by MALDI MSI for distribution of MBP. (e) H&E stained adjacent kidney tissue of nanoDESI analysis. (f) Raw nanoDESI MSI visualized HBA at 200 μm spatial resolution. (g) Predicted high spatial resolution molecular distribution of HBA after applying image fusion. (h) Adjoining sections of kidney sections mapped by MALDI MSI for distribution of HBA.

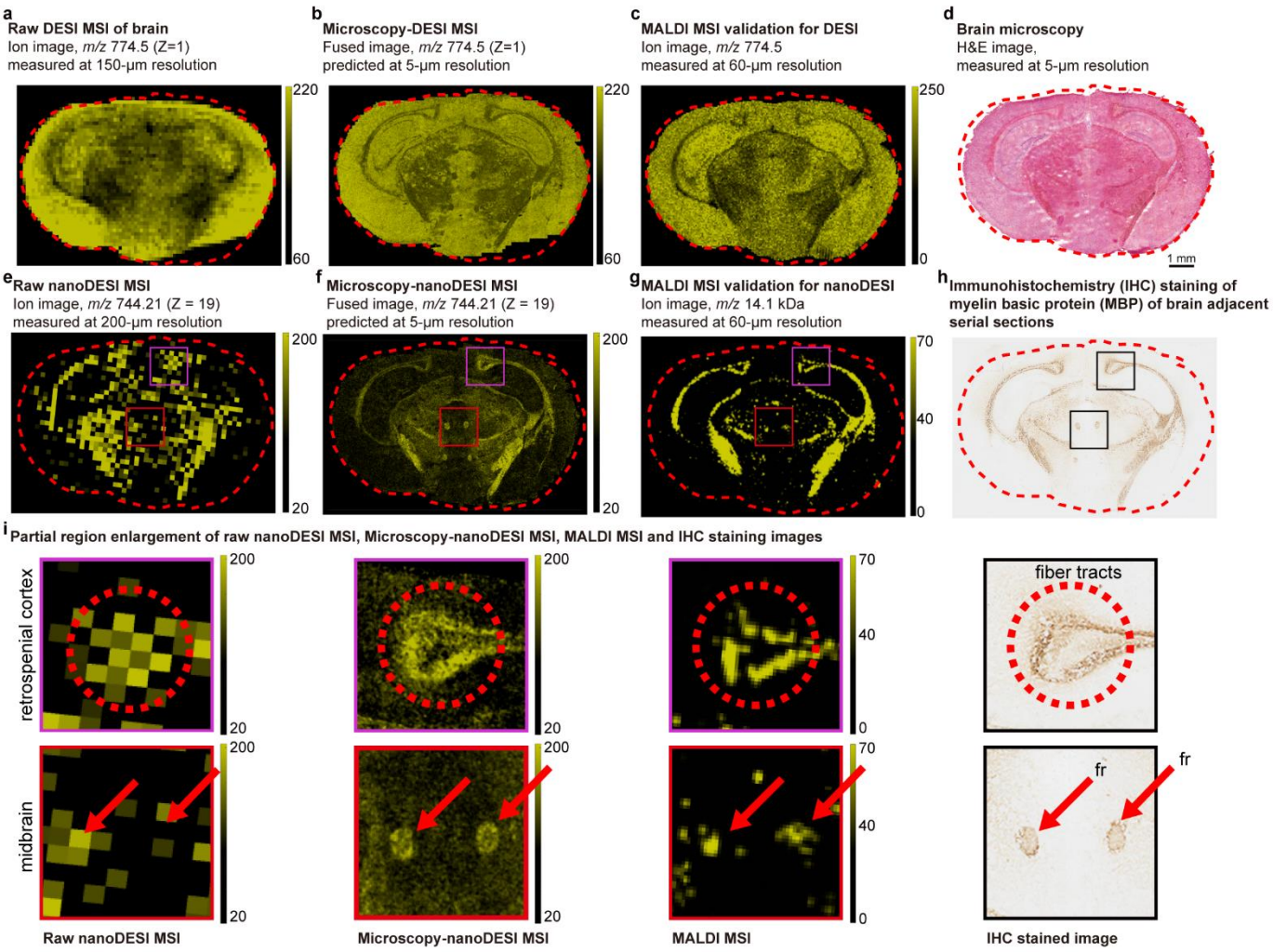

Fig. 5 Brain serial section of DESI, nanoDESI, MALDI and immunohistochemistry mapping. (a) Raw DESI MSI analysis of lipid species. (b) Predicted high spatial resolution MSI of DESI analysis after applying image fusion. (d) Ion distribution validation by MALDI analysis. (d) H&E stained serial section. (e) Raw nanoDESI MSI analysis of myelin basic protein. (f) Predicted high spatial resolution MSI of nanoDESI analysis after applying image fusion. (g) Ion distribution validation by MALDI analysis. (h) Immunohistochemistry (IHC) staining of myelin basic protein. (i) Enlarged images of raw nanoDESI MSI, MSI-microscopy image, MALDI MSI and IHC staining.

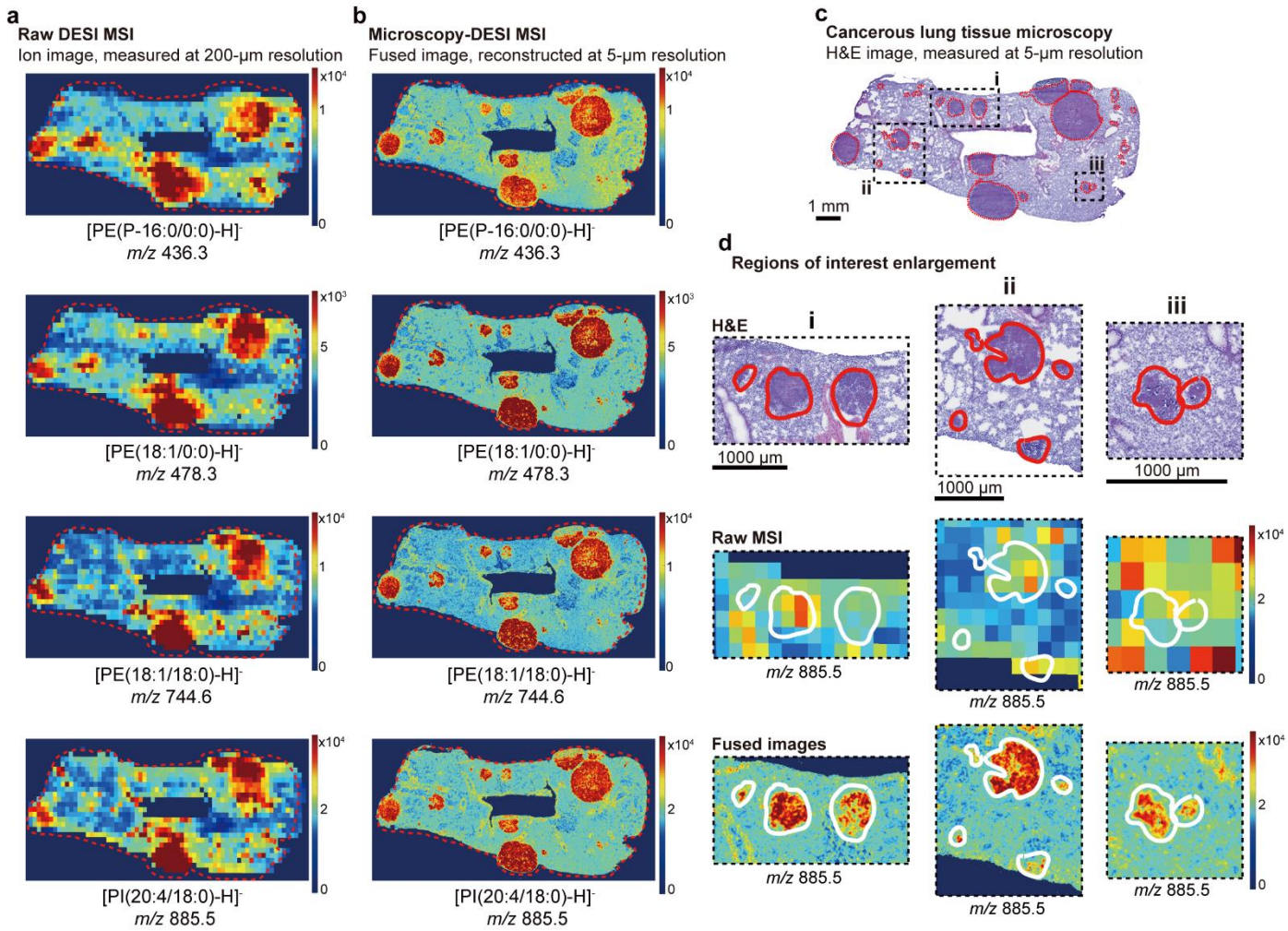

Fig. 6 Cancerous lung tissue section analysis. DESI MSI was conducted under negative mode for depicting lipids species of the metastatic breast cancer tissue section of mouse lung. (a) Raw DESI-MSI of lipid species. (b) Predicted high spatial resolution MSI after applying image fusion. (c) H&E stained lung tissue section. The cancerous regions are circled in red by the pathologist. (d) Enlarged images of microscopy image, raw DESI MSI and MSI-microscopy image of [PI(20:4/18:0)-H]$^-$ species.

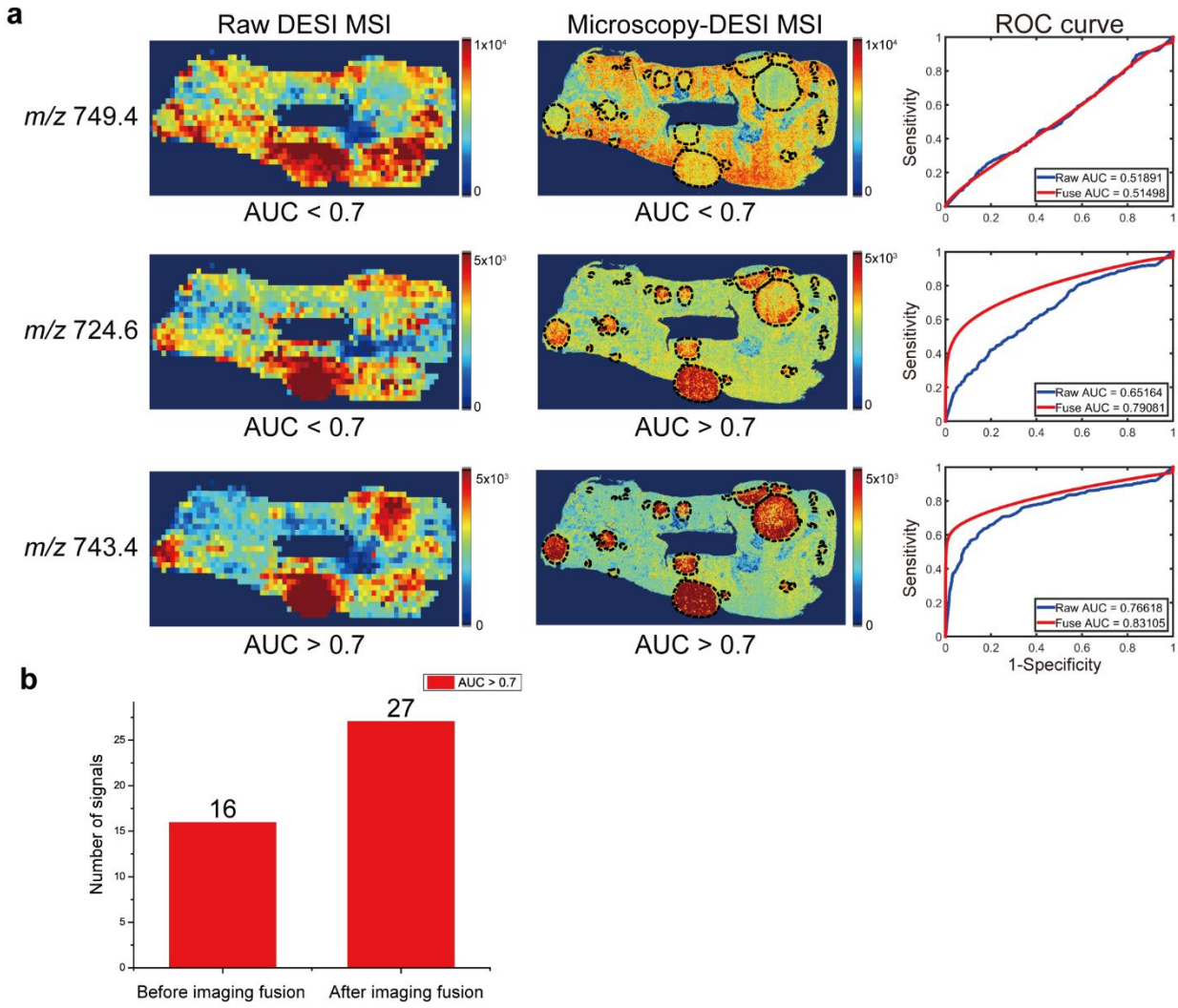

Fig. 7 Potential biomarker for cancerous tumor margin determination using ROC examination. (a) For *m/z* 749.4, AUC was lower than 0.7 before and after image fusion. For *m/z* 724.6, the AUC was lower than 0.7 before image fusion and higher than 0.7 after image fusion. For *m/z* 743.4, the AUC was higher than 0.7 before and after image fusion. The cancerous regions were circled in black. (b) After applying image fusion, number of potential biomarkers (the signals with AUC larger than 0.7) increased by 11.